# DESIGN AND ANALYSIS OF FEEDBACK CONTROLLER FOR WPT-PV-FED DUAL-INPUT ONBOARD EV CHARGER USING JAYA OPTIMIZATION ALGORITHM

**Ganesh Babu. M* – P. Srinivasa Rao Nayak**

*Department of Electrical and Electronics Engineering, National Institute of Technology Tiruchirappalli, Tamil Nadu 620015, INDIA.*

**ARTICLE INFO**

***Article history*:**
*Received: 12. 2. 2025.*
*Received in revised form: 27. 5. 2025.*
*Accepted:27. 5. 2025.*

***Keywords:***
*Dual-input buck boost converter (DIbB)*
*Dual-input converter (DIC)*
*Electric Vehicles (EVs)*
*JAYA algorithm*
*Receiver (Rx)*
*Transmitter (Tx)*
*Wireless Power Transfer (WPT)*

*DOI: 10.30765/er.2824*

***Abstract:***

*The demand for robust and reliable electric vehicle (EV) charging infrastructure has accelerated the exploration of advanced charging systems utilizing multiple energy sources. In this context, a dual-input EV charger powered by Wireless Power Transfer (WPT) and Photovoltaic (PV) sources is proposed in this paper. The charger system employs a Proportional-Integral (PI) controller to regulate the output voltage by comparing it with the required battery charging voltage. Given the nonlinear and time-varying nature of the input sources, tuning the controller using conventional methods proves inadequate. Therefore, a metaheuristic-based optimization technique, known as the JAYA algorithm, is utilized to determine the optimal PI controller parameters for improved voltage regulation. The closed-loop system performance is verified through MATLAB/SIMULINK simulations, and further validated using a laboratory-developed prototype controlled via an FPGA platform. The results demonstrate that the JAYA-tuned controller significantly enhances transient performance and voltage stability under various input fluctuations and load disturbances. The practical implementation confirms the effectiveness of the proposed system, offering a viable solution for next-generation EV charging applications..*

## 1 Introduction

The global shift from Internal Combustion Engine (ICE) vehicles to Electric Vehicles (EVs) is motivated by environmental sustainability, energy security, and fossil fuel depletion concerns, alongside efforts by governments, industries, and organizations to reduce carbon emissions in response to climate change. A primary challenge to EV adoption is the lack of convenient, sustainable charging infrastructure and range anxiety. Most of the existing charging infrastructure is plug-in charging [1] based, it is a mature and compatible mode of charging across EV models, but faces challenges such as physical degradation of connectors, safety hazards from exposed terminals, and inconvenience to users through manual handling particularly in extreme weather conditions. These drawbacks bring attention to the necessity of a more dependable, user-centric solution. Consequently, Wireless Power Transfer (WPT) [2] presents itself as a potential substitute, providing contactless, automated charging which improves safety, convenience, and robustness. Moreover, WPT enables dynamic charging, allowing EVs to charge while in motion, which significantly reduces range anxiety and supports continuous mobility, but requires a very high infrastructure cost. So, a WPT based charging system integrated with a on-board roof-top PV system energy serves the advantage of

* Ganesh Babu. M
*E-mail address:ganeshphdnitt@gmail.com*

sophisticated charging and solves the range anxiety problem of the EV [3]. However, combining WPT and PV systems for EV charging is challenged by the variability of solar output [4] and WPT's sensitivity to coil misalignment [5], necessitating consistent voltage regulation to protect battery health [6]. To overcome these problems, multi-input single output (MISO) [7] converters are employed which offer flexible integration of multiple energy sources with efficient power management and reduced component count. They enhance system reliability, support renewable inputs, and provide source redundancy for uninterrupted output.

Among multiple-input single-output (MISO) converter configurations, non-isolated dual-input converters (DICs) are particularly favored due to their superior efficiency, compact size, cost-effectiveness, and better dynamic response compared to isolated alternatives. Various DIC architectures have been proposed for integrating multiple energy sources in electric vehicle (EV) charging applications, yet many exhibit notable shortcomings. For instance, the converter in [8] is limited to specific operating modes buck-boost or individual buck/boost and does not support bidirectional energy flow. An improvement was suggested in [9] by introducing an extra switch to enable reverse power transfer, but its scope was confined to storage-to-load scenarios. The solution in [10] supported mode transitions and bidirectional operation using relays and diodes, though it suffered from increased mechanical complexity and decreased system reliability. A more integrated approach in [11] eliminated the use of relays and facilitated all modes with bidirectional flow; however, it did not adequately address control challenges arising from fluctuating sources such as PV and WPT systems. High-complexity designs like the coupled-inductor-based topology in [12] present difficulties in controller implementation, while the solutions in [13] and [14] are either suitable only for low-voltage systems or lack simultaneous dual-source energy merging capabilities. These limitations highlight the necessity for a converter that balances compact design, mode versatility, and robust control performance. The dual-input single-output (DISO) converter proposed in this study fulfills these criteria. It employs a single inductor, three switches, and three diodes to support dual-input boost (DIB), dual-input buck (DIBK), and dual-input buck-boost (DIbB) modes. A PI controller, designed using a small-signal model of the converter, maintains output voltage stability under varying source conditions [15]. The hardware implementation described in [16] demonstrates the converter's capability to efficiently integrate both WPT and PV inputs without relying on relays or complex magnetic components, making it well-suited for practical EV charging deployments.

Effective control of DISO converters is crucial for managing power flow from multiple sources, maintaining stable output voltage, and ensuring efficient and reliable operation especially in EV charging systems. In [17], a DISO converter capable of operating in buck, boost, and buck-boost modes is used to integrate an energy source and a battery to supply the desired load. A Lyapunov control strategy is applied for closed-loop operation of the converter, ensuring global stability and offering fast dynamic response. However, it faces challenges such as design complexity, sensitivity to model inaccuracies, and a lack of dynamic performance optimization. Its implementation is also computationally intensive, limiting practicality in real-time DISO converter applications. Similarly, in [18], a DISO converter operating as a bidirectional buck and boost converter is controlled using a sliding mode control strategy. Although its performance is more robust than the conventional PI controller, it suffers from chattering effects, complex design requirements, and sensitivity to measurement noise, which may pose challenges in real-time digital implementation. Reference [19] proposes a super twisting control strategy to mitigate the chattering effect observed in [18], but this approach also involves complex gain tuning and higher computational load. Its performance can still be affected by system uncertainties and measurement noise. Likewise, in [20], a backstepping controller with a nonlinear disturbance observer is implemented to minimize overshoot and undershoot across various operating modes. While this method ensures strong stability and fast voltage regulation, it demands precise modeling and intricate controller design. The main limitations of these sophisticated nonlinear control methodologies are their complexity, making them difficult for implementation. There exists a strong requirement for easier, yet efficient control methods that ensure ease of implementation and adequate performance. Here, optimizing a conventional PI controller offers a practical and effective solution. Optimization-based tuning allows for parameter selection for the controller in a systematic way to enhance the transient response, minimize overshoot, and ensure robustness against input variations of particular interest for complicated systems such as dual-input EV chargers.

Several recently developed bio-inspired algorithms such as Particle Swarm Optimization (PSO) [21], Ant Colony Optimization (ACO) [22], and Genetic Algorithm (GA) [23] have been widely adopted for designing feedback controllers in various power converter applications. In contrast, conventional tuning methods like the Ziegler-Nichols (Z-N) approach, while simple and easy to implement, suffer from limitations including dependence on sustained oscillations, inadequate tuning under dynamic source/load conditions, and poor transient performance characterized by high overshoot and longer settling times. These drawbacks make Z-N-based controllers less effective for modern electric vehicle (EV) charging systems, especially those involving dual-input configurations with variable sources like photovoltaic (PV) and wireless power transfer (WPT). To address these limitations, optimization-based tuning offers a more adaptable and robust control strategy. Among these, the JAYA algorithm has recently gained attention for its simplicity, parameter-free nature, and ability to achieve fast convergence and reliable performance across diverse optimization problems [24][25]. Robust controllers such as 2-Degree of Freedom (2-DOF) and Fractional Order Proportional–Integral–Derivative (FOPID) have been developed using JAYA for high-performance systems like magnetic levitation (maglev), providing insights into enhancing EV charging stability [26]. Motivated by these strengths, this work employs the JAYA algorithm to optimize a PI controller for a non-isolated Dual-Input Single-Output (DISO) converter and presents a comparative analysis with the Z-N method to demonstrate the advantages of modern optimization-based control.

Hence, this paper focuses on the design of a feedback controller for a non-isolated Dual-Input Single-Output (DISO) EV charger, with a comprehensive performance analysis under various input and load disturbances. These include coil misalignments in the wireless power transfer (WPT) system, solar voltage fluctuations caused by partial shading of photovoltaic panels, and variations in battery reference voltages. A simple Proportional-Integral (PI) controller is proposed for regulating the DISO converter, with its parameters optimized using the JAYA optimization algorithm, based on the small-signal modeling of the converter. The performance of the optimized controller is experimentally validated on a hardware test bench using an FPGA-based controller. Its effectiveness is evaluated and compared against the conventional Ziegler-Nichols tuning method under various input and load voltage fluctuation scenarios. The comparison is based on key transient performance metrics, including peak overshoot, settling time, rise time, and Integral of Time-weighted Absolute Error (ITAE), demonstrating the superior performance of the proposed optimized controller.

This paper is organized as follows: Section 2 provides a in detailed modeling of the proposed dual-input EV charger, with dual energy fed sources such as wireless power transfer (WPT) and photovoltaic (PV) systems, and JAYA optimization algorithm-based feedback controller design. Section 3 describes the hardware setup of the systems. Section 4 presents the performance analysis of the system based on proposed feedback controller and transients, comparison analysis of the proposed algorithms with conventional Ziegler-Nichols method. Section-5 presents the conclusion of the paper.

## 2 JAYA ALGORITHM BASED PI CONTROLLER DESIGN

### *2.1 Modeling of PV-WPT sources fed Dual-Input EV charger with PI controller*

Dual-input sources refer to the integration of renewable energy systems into EV charging setups. An EV charger with dual inputs might draw power from both the electrical grid and renewable sources such as solar panels or wind turbines. This setup allows the charger to utilize renewable energy when available, reducing the environmental impact of the charging process. In this design, a dual-input on-board EV charger is proposed, with wireless power transfer (WPT) serving as the primary energy source and a rooftop photovoltaic (PV) panel mounted on the vehicle acting as the secondary source. The block diagram and schematic of the proposed dual-input EV charger are shown in Figs. 1a and 1b, respectively. The modeling of the input sources and the on-board EV charger is described in the upcoming sections.

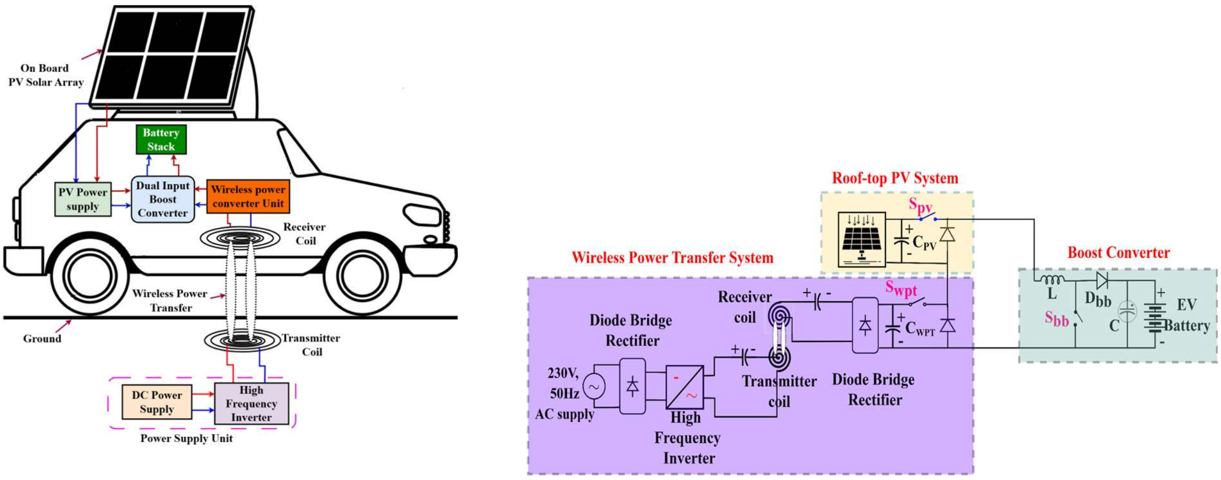


*(a)* *(b)*

*Figure 1. Dual-input EV charger. (a) Block diagram of the dual-input charging system. (b) Schematic Diagram of the Dual-Input On-board EV charger.*

#### *2.1.1 PV system*

The PV system can be installed either on the rooftops of vehicles or on parking shelters to capture sunlight and convert it into electrical energy. The basic equivalent circuit of a photovoltaic (PV) module, based on the single-diode model, is shown in Fig. 2. This equivalent circuit includes key components such as a photocurrent source, a diode, and resistive elements, among others.

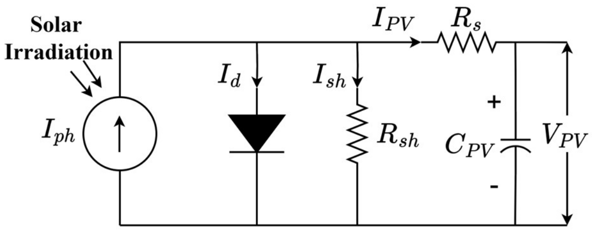


*Figure 2. Equivalent circuit of PV cell.*

The total current ($I_{PV}$) and voltage ($V_{PV}$) are supplied to the EV charger. In the solar module, the photocurrent ($I_{ph}$), diode current ($I_d$, and the currents through the series and shunt resistances ($I_{rs}$ and $I_{sh}$, respectively) are represented by Equations (1) and (2).

$$\begin{cases} I_{PV} &= I_{ph} - I_d - I_{sh} \\ I_{ph} &= I_L\left(1 - \frac{T}{T_{ref}}\right) \\ I_d &= I_o\left(\exp\left(\frac{qV_d}{nkT}\right) - 1\right) \\ I_{sh} &= \frac{V_{PV} + I_{PV}R_s}{R_{sh}} \end{cases} \tag{1}$$

$$V_{PV} = \left(\frac{kT\ \ s}{q}\right) \times \ln\left(\left(\frac{I_L}{I_0}\right) + 1\right) \tag{2}$$

The relationship between $V_{PV}$ and $V_d$ is, $V_d = V_{PV} + I_{PV} * R_s$ . As the voltage drop across the series resistance ($R_s$) is very low (as $R_s \approx 0$), hence $V_{PV} \approx V_d$.
where, $V_{PV}$ is open circuit voltage across the solar cell, $I_{PV}$ is PV cell output current, $I_{Ph}$ is photo current, $I_L$ is the light generated current, $I_d$ is diode current, $I_{sh}$ is the shunt resistance current, $V_d$ is diode forward voltage, *n* is the ideality factor, *k* is the Boltzmann constant, *T* is the reference temperature, $R_s$ & $R_{sh}$ are the series and the shunt resistance respectively and $C_{PV}$ is the parallel capacitor to eliminate high frequency components in the PV system which is fed into the DIbB converter input.

### *2.1.2 WPT system*

Wireless power transfer (WPT) is an emerging technology used to transfer electrical energy from a transmitter to a receiver without physical connections, utilizing various methods and technologies that rely on time-varying electric, magnetic, or electromagnetic fields. In the system, the rectified grid source is fed to the inverter through a DC link. The inverter converts the DC power into high-frequency AC, which is then supplied to the transmitter coil via a compensation network. The high-frequency AC received by the compensated receiver coil is rectified and delivered to the EV charger. The power flow diagram and basic circuit model of the WPT system are shown in Fig. 3a and 3b. To enhance active power transfer, series-series compensation is applied, where two external capacitors, $C_1$ and $C_2$, are connected in series with the primary and secondary windings of the system. This configuration improves the overall efficiency and performance of the WPT system. The series–series (S–S) compensated high-frequency AC signal from the receiver coil (*Rx*) is passed through a filter capacitor ($C_{WPT}$) before entering the DIbB converter. This capacitor effectively attenuates high-frequency components and minimizes voltage ripple, ensuring a smoother DC input for the converter.

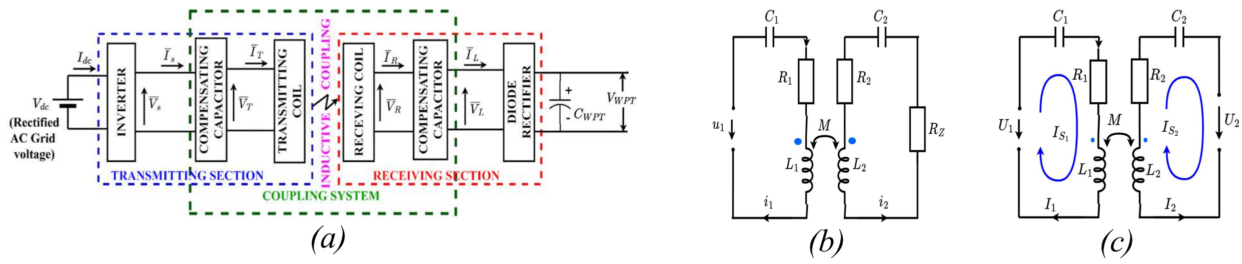


*Figure 3. (a) Power flow block diagram of the WPT system. (b) Simplified circuit for series–series compensation. (c) Circuit suited for loop current analysis.*

Here, the WPT system model represented in [27] is shown through equations below: As shown in Fig. 3c, $U_1$ is high frequency single phase inverter output fundamental RMS voltage and is given by Equation (3).

$$U_1 = \frac{2\sqrt{2}}{\pi} U_{ml} \tag{3}$$

Where, $U_{ml}$ is the amplitude of the high frequency single phase inverter whose output has a rectangular voltage profile. The loop currents analysis is given below, and the WPT system model is represented through Equations (4) - (6) as shown below.

$$-u_1 + \frac{1}{C_1}\int_0^t i_1 dt + u_{C_1}(0) + R_1 i_1 + L_1 \frac{di_1}{dt} + M \frac{di_2}{dt} = 0 \tag{4}$$

$$-L_2 \frac{di_2}{dt} + M \frac{di_1}{dt} + R_2 i_2 - \frac{1}{C_2}\int_0^t i_2 dt - u_{C_2}(0) - R_z i_2 = 0 \tag{5}$$

$$\begin{bmatrix} I_{S_1} \\ I_{S_2} \end{bmatrix} = \begin{bmatrix} R_1 + j\left(\omega L_1 - \frac{1}{\omega C_1}\right) & -j\omega M \\ -j\omega M & R_2 + R_Z + j\left(\omega L_2 - \frac{1}{\omega C_2}\right) \end{bmatrix} \times \begin{bmatrix} \tilde{i}_L \\ \tilde{v}_C \end{bmatrix} \tag{6}$$

The receiver output voltage ($U_2$) is given by,

$$U_2 = j\omega M I_{S_1} + R_2 I_{S_2} + I_{S_2}\left(-j\omega L_2 + \frac{j}{\omega C_2}\right) \tag{7}$$

The diode bridge rectified output voltage (i.e., $V_{wpt}$) is given by,

$$V_{wpt} = \frac{2\sqrt{2}U_2}{\pi} \tag{8}$$

### *2.1.3 Dual Input EV Charger*

The equivalent circuit diagram of the proposed dual-input on-board EV charger is shown in Fig. 4a. The input sources, PV and wireless power transfer (WPT), are connected to a DC-DC converter, operating as buck-boost converter to ensure that the input sources provide the required rated voltage for EV charging. The modes of operation for the buck-boost configuration are depicted in Figs. 4b-4e, with the corresponding timing diagram in Fig. 4f.

- Mode-I: In this mode, the load is powered entirely by the capacitor. The WPT system is connected by turning ON switches $S_{wpt}$ and $S_{bb}$, allowing energy to be stored in the inductor through diode $D_{pv}$.
- Mode-II: In this mode, the output capacitor continues to supply power to the load. Switches $S_{pv}$, $S_{wpt}$, and $S_{bb}$ operates to link both the WPT and PV sources, thereby storing energy in the inductor.
- Mode-III: Similarly, in this mode, the load is powered by the capacitor, while the inductor is charged solely by the PV source through the operation of switches $S_{pv}$, and $S_{bb}$, and diode $D_{pv}$.

- Mode-IV: In this mode, both sources are isolated from the load, and switch $S_{bb}$ is OFF. The energy stored in the inductor is discharged to the load through diodes $D_{wpt}$. and $D_{pv}$.

The switching patterns for the different modes of operation are outlined in Table 1.

*TABLE 1. Switching Pattern of the Dual-Input Converter for Different Buck-Boost Operation Modes.*

| **Converter Modes of Operation** | $S_{pv}$ | $D_{pv}$ | $S_{wpt}$ | $D_{wpt}$ | $S_{bb}$ | $D_{bb}$ |
|---|---|---|---|---|---|---|
| **Mode-I** | OFF | ON | ON | OFF | ON | OFF |
| **Mode-II** | ON | OFF | ON | OFF | ON | OFF |
| **Mode-III** | ON | OFF | OFF | ON | ON | OFF |
| **Mode-IV** | OFF | ON | OFF | ON | OFF | ON |

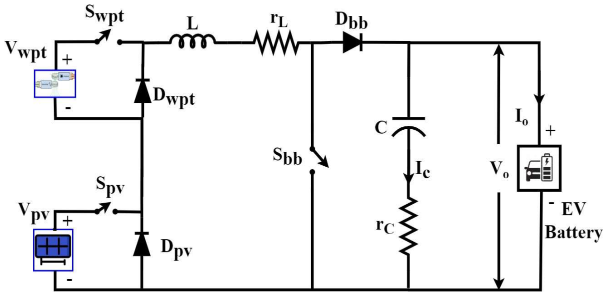


*(a)*

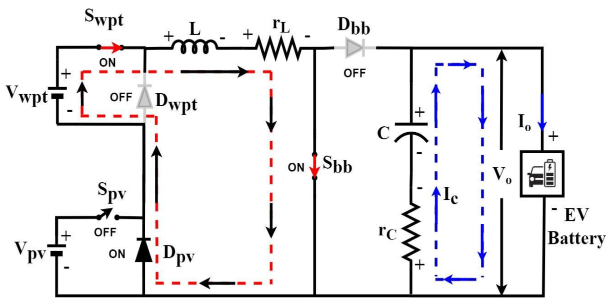


*(b)*

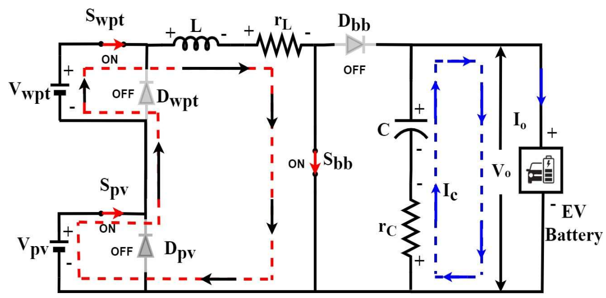


*(c)*

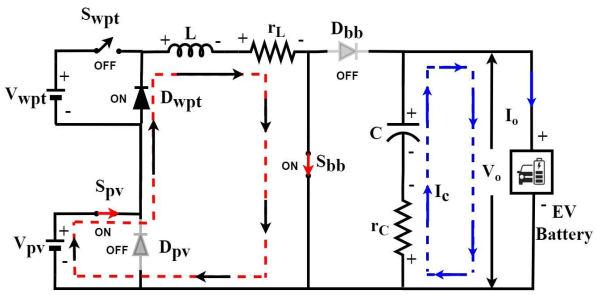


*(d)*

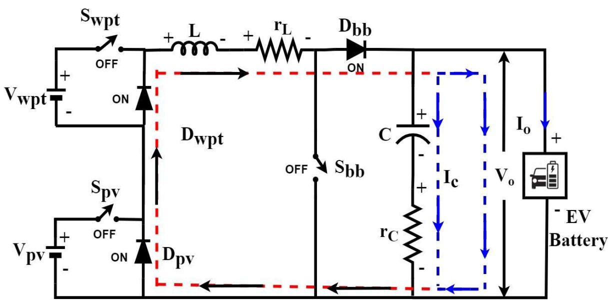


*(e)*

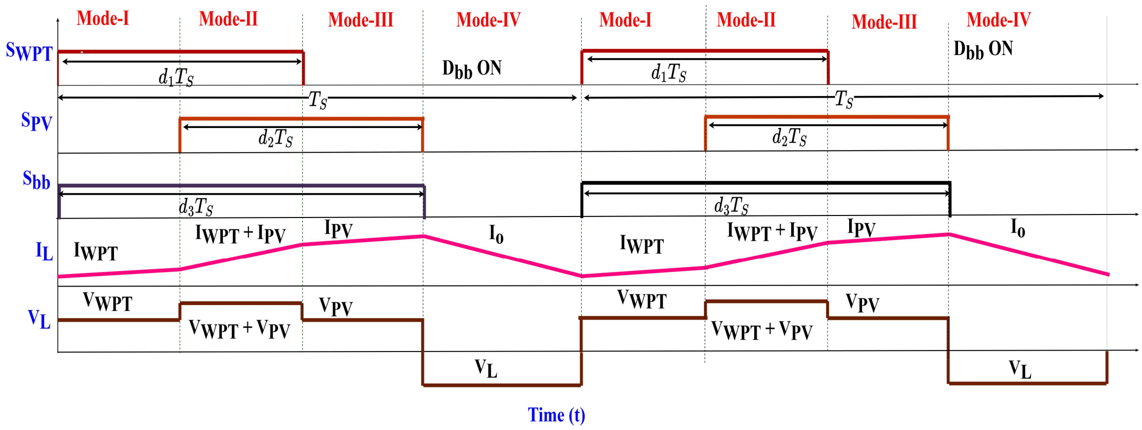


*(f)*

*Figure 4. (a) Overall circuit diagram of Dual input converter. (b) Mode-I operation. (c) Mode-II operation. (d) Mode-III operation. (e) Mode-IV operation. (f) Timing diagram of Dual-Input buck-boost converter.*

## *2.2 Mathematical modelling of the converter*

The state-space model of Dual input Buck Boost (DIbB) converter is given below.

$$\begin{bmatrix} L & 0 \\ 0 & C \end{bmatrix}\begin{bmatrix} \tilde{\imath}_L \\ \tilde{v}_c \end{bmatrix} = \begin{bmatrix} 0 & -1 + (d_1 + d_2 + d_3) \\ 1 - (d_1 + d_2 + d_3) & \frac{-1}{R} \end{bmatrix}\begin{bmatrix} \tilde{\imath}_L \\ \tilde{v}_c \end{bmatrix} \tag{10}$$

$$+ \begin{bmatrix} V_{WPT} + V_C \\ -I_L \end{bmatrix}\tilde{d}_2 + \begin{bmatrix} V_{PV} + V_{WPT} + V_C \\ -I_L \end{bmatrix}\tilde{d}_3$$

$$\begin{bmatrix} v_o \\ i_1 \\ i_2 \\ i_3 \end{bmatrix} = \begin{bmatrix} 0 & -1 \\ d_1 & 0 \\ d_2 & 0 \\ d_3 & 0 \end{bmatrix}\begin{bmatrix} \tilde{\imath}_L \\ \tilde{v}_c \end{bmatrix} + \begin{bmatrix} 0 & 0 \\ 0 & 0 \\ 0 & 0 \\ 0 & 0 \end{bmatrix}\begin{bmatrix} \tilde{v}_{PV} \\ \tilde{v}_{WPT} \end{bmatrix} + \begin{bmatrix} 0 \\ I_L \\ 0 \\ 0 \end{bmatrix}\tilde{d}_1 + \begin{bmatrix} 0 \\ 0 \\ I_L \\ 0 \end{bmatrix}\tilde{d}_2 + \begin{bmatrix} 0 \\ 0 \\ 0 \\ I_L \end{bmatrix}\tilde{d}_3 \tag{11}$$

For obtaining the equivalent signal model the state Equation (10) is expanded and is given below:

$$\begin{aligned} L\frac{dI_L}{dt} &= -(1 - d_1 - d_2 - d_3)\tilde{v}_c + (d_1 + d_3)V_{PV} + (d_2 + d_3)V_{WPT} \\ &+ (V_{PV} + V_C)\tilde{d}_1 + (V_{WPT} + V_C)\tilde{d}_2 + (V_{PV} + V_{WPT} + V_C)\tilde{d}_3 \end{aligned} \tag{12}$$

$$C\frac{dV_C}{dt} = (1 - d_1 - d_2 - d_3)\tilde{\imath}_L - \frac{1}{R}\tilde{v}_c - I_L\tilde{d}_1 - I_L\tilde{d}_2 - I_L\tilde{d}_3 \tag{13}$$

Similarly, the Equation (11) to form output equation as below,

$$\begin{aligned} v_o &= -v_c; i_1 = d_1\tilde{\imath}_L + I_L\tilde{d}_1 \\ i_2 &= d_2\tilde{\imath}_L + I_L\tilde{d}_2; i_3 = d_3\tilde{\imath}_L + I_L\tilde{d}_3 \end{aligned} \tag{14}$$

The proposed system equivalent small signal modal circuit is shown in Fig. 5, and the transfer function of the small signal model of the proposed system is given below:

$$\frac{\tilde{v}_C(s)}{\tilde{d}_1(s)} = \frac{[1-(d_1+d_2+d_3)](V_{PV}+V_C)-sLI_L}{s^2LC+s\frac{L}{R}+[1-(d_1+d_2+d_3)]^2} \tag{15}$$

$$\frac{\tilde{v}_C(s)}{\tilde{d}_2(s)} = \frac{[1-(d_1+d_2+d_3)](V_{WPT}+V_C)-sLI_L}{s^2LC+s\frac{L}{R}+[1-(d_1+d_2+d_3)]^2} \tag{16}$$

$$\frac{\tilde{v}_C(s)}{\tilde{d}_3(s)} = \frac{[1-(d_1+d_2+d_3)](V_{PV}+V_{WPT}+V_C)-sLI_L}{s^2LC+s\frac{L}{R}+[1-(d_1+d_2+d_3)]^2} \tag{17}$$

The inputs to this model include three duty cycles, $d_1$, $d_2$ and $d_3$, along with the source voltages $V_{PV}$ and $V_{WPT}$ . The duty cycles are adjusted by the PI controller. The model evaluates the converter's output voltage $V_o$ (i.e., $V_T$ ), compares it to the rated voltage, and computes the error, which is then fed into the PI controller. The PI controller calculates the necessary adjustments to the duty cycles $\tilde{d}_1$, $\tilde{d}_2$, and $\tilde{d}_3$. The initial values for the duty cycles, $d_{01}$, $d_{02}$ and $d_{03}$, are carefully chosen to ensure optimal performance.

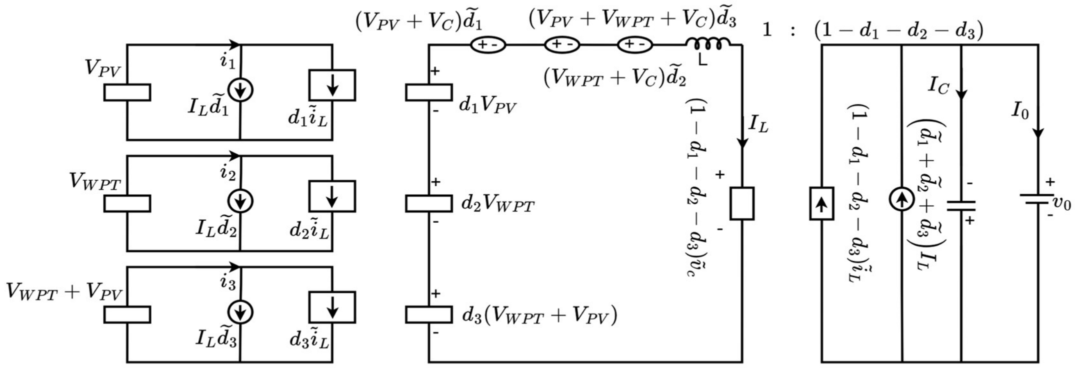


*Figure 5. Proposed system equivalent small signal model circuit.*

### *2.3 Problem formulation:*

The block diagram of the EV battery charger with a PI controller is illustrated in Fig. 6. The objective is to determine the optimal values for $K_p$ and $K_i$ to ensure the output voltage of the EV charger remains constant throughout the battery charging process. If $V_{ref}$ is the rated output voltage of the charger and $V_o$ is the instantaneous output voltage, constant voltage charging can be achieved by maintaining $V_o$ equal to $V_{ref}$ . Let the error be defined as $(e) = V_{ref} - V_o$, representing the difference between the rated and actual output voltages of the charger. The goal is to find the optimal values for the controller constants $K_p$ and $K_i$ that minimize this error. This task can be formulated as an optimization problem, as shown in Equation (18) with the objective to minimize the error subject to certain constraints.

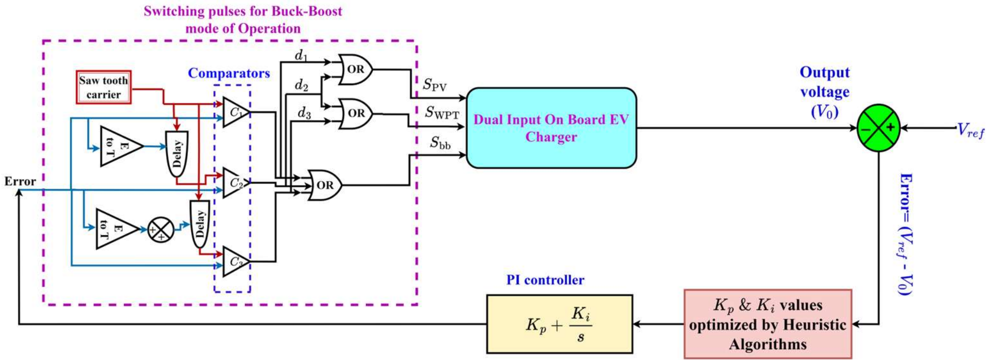


*Figure 6. Block diagram of the Dual-Input On-Board EV charger with feedback Controller.*

$$F(\Psi) \quad = \int_0^{t_{\text{sim}}} t \cdot |V_{\text{ref}} - V_o| \, dt \tag{18}$$

$$\Psi_{(lower)} \leq \Psi \leq \Psi_{(upper)}$$

where, $t_{sim}$ = simulation time, $t$ = Structural Interval and, $\Psi$ = $K_p$, $K_i$ in the controller structure. It may be noted that the minimum and maximum values of $K_p$ and $K_i$ are obtained using the small signal model developed in Equations (15)- (17).

### *2.4 PI controller parameters Optimization through JAYA Algorithm*

The JAYA algorithm is a metaheuristic optimization algorithm based on swarm intelligence; it is a parameter-free optimization method that iteratively improves candidate solutions. Named after the Sanskrit word for "victory," it aims to move towards success by optimizing solutions based on their performance. It updates each solution by moving towards the best and away from the worst in the population, effectively balancing exploration and exploitation. Various steps through which the PI controller parameters are optimized is shown as a flowchart in the Fig. 7a and the parameters updation process in shown graphically in the Fig. 7b below,

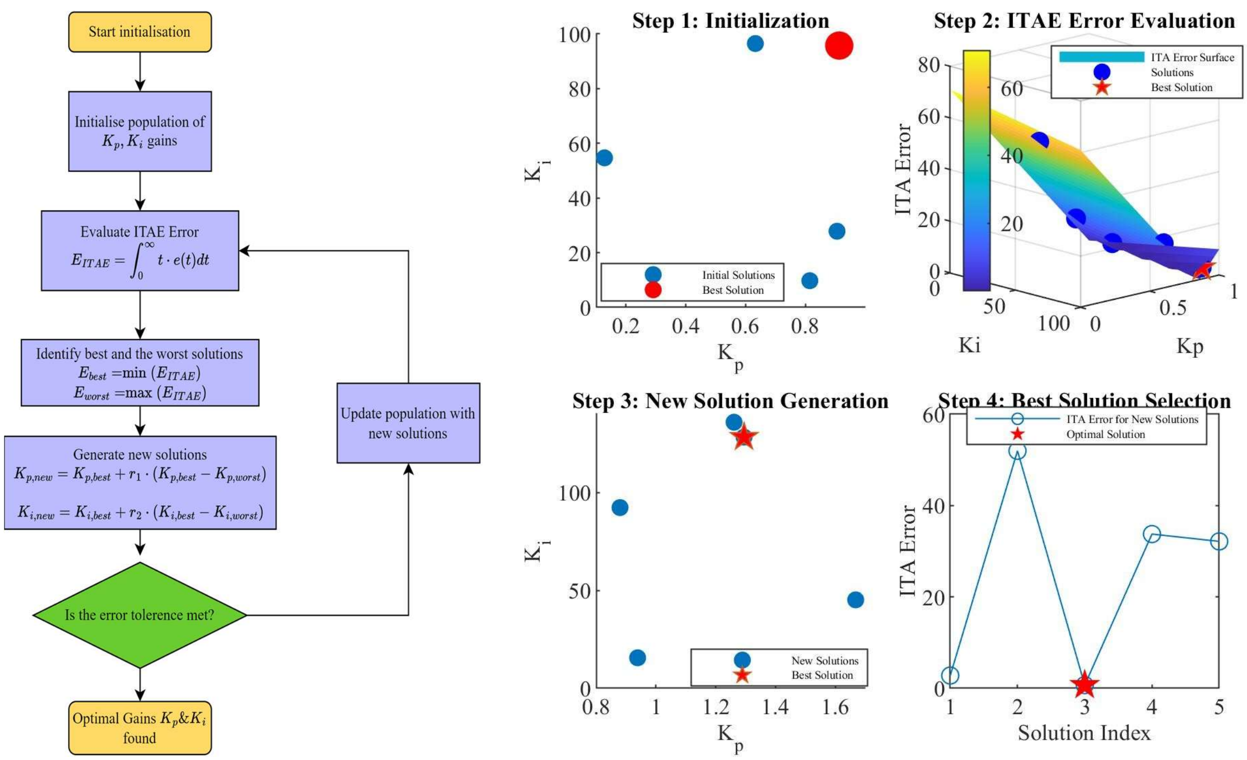


*(a)* *(b)*

*Figure 7. (a) JAYA algorithm Flowchart. (b) $K_p$, $K_i$ Parameters updation for proposed dual-input EV charger.*

## 3 HARDWARE DESCRIPTION

The experimental setup comprises a PV system, a WPT system, and a dual-input EV charger with buck-boost functionality. A SM100-AR-75 solar emulator is used to simulate the PV system, capable of adjusting voltage (0-100V) and current (0-16A). It supports digital constant voltage (CV) and constant current (CC) modes, with an Ethernet (100 Mb/s, RJ45) and USB interface for data exchange. The WPT system consists of an H-bridge inverter using SCH2080KE SiC MOSFETs (1200V, 40A, 1 MHz), Litz wire coils (0.177 mH), and a polarized capacitor bank (18.75 nF) for compensation. Power is rectified by an MUR30120 ultra-fast recovery rectifier.

The dual-input converter uses SKM 75GB063D IGBTs (600V, 100A), a 5 mH iron-core inductor, and a 2200 µF electrolytic capacitor (450V). The EV battery bank consists of five 12V, 6AH LiFePO4 batteries (71V total). A Hall effect sensor (HE055T01) and IC7440 measure currents and voltages, amplified by AD8022 op-amps and digitized via an AD7366 ADC. A SPARTAN-6 FPGA and XILINX CPLD (XC2C258) generate PWM signals, while a CY7C68013A USB microcontroller provides communication. Code is uploaded using the XILINX ISE design suite via JTAG. The complete hardware setup is shown in Fig. 8.

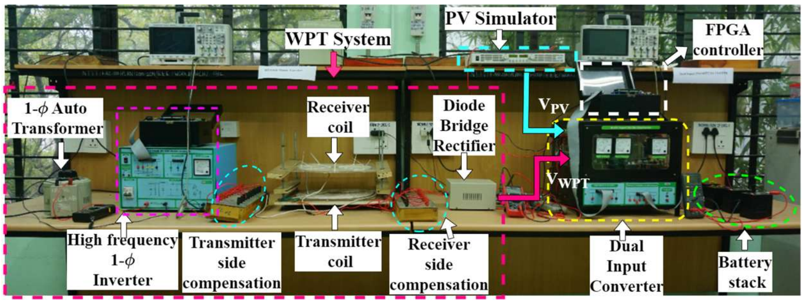


*Figure 8. Hardware setup of the dual-input on-board EV charger.*

## 4 RESULTS & DISCUSSION

A custom MATLAB program has been developed for designing the feedback controller using the JAYA algorithm. The parameters for the JAYA algorithm were determined through trial and error, as detailed in Table 2. Since JAYA is a population-based optimization technique, Fig. 9 shows the evolution of the objective function value for the best control parameters over iterations. The convergence is rapid, with the objective function value (ITA error) reaching as low as 0.0075692 after 30 iterations. Consequently, the optimized feedback controller constants are found to be $K_P$ = 0.2449 and $K_I$ = 14.8089 following these 30 iterations.

*Table 2. JAYA Algorithm Parameters Considered During Optimization.*

| **Parameter** | **Value** |
|---|---|
| Population Size | 30 |
| Iterations | 30 |
| $r$, $r_1$, $r_2$ (Random Numbers) | [0, 1] |

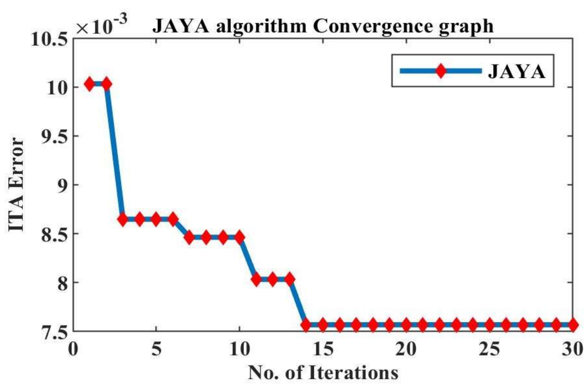


*Figure 9. Convergence graph of the JAYA algorithm.*

The FPGA-based dual-input on-board EV charger, as shown in Fig. 1b, was developed in the laboratory for the purpose of charging the EV battery at a constant voltage. Waveforms were recorded during testing, and the measured results are presented alongside the simulation results, covering various cases based on the connected input sources. The analysis considers several parameters, including $V_{WPT}$ (input voltage from the WPT system to the DIbB converter), $V_{PV}$ (input voltage from the PV system to the DIbB converter), $V_T$ (terminal voltage of the DIbB converter), $I_{bat}$ (output current of the DIbB converter, or the EV battery charging current), $V_{Rx}$ (receiver coil voltage), and $I_{Rx}$ (receiver coil current).

*4.1 Performance analysis of the Dual-Input EV charger*

*4.1.1. Case-I(a) (No change in the Input, Output parameters)*: In this case, the operation of the proposed charger, utilizing the JAYA algorithm-optimized control parameters, is observed while charging the EV battery at a constant voltage of 71V. This is achieved with a perfectly aligned *Tx* and *Rx* coil setup in the WPT system, resulting in a constant $V_{WPT}$, and a PV system operating under constant irradiation of 1000 $W/m^2$, with six solar panels of 6V each, connected in series forming a string accounting to a voltage $V_{PV}$ of 36V. The input voltages to the DIbB converter, along with the output EV battery charging voltage and current, are illustrated in Fig. 10a additionally, the high-frequency voltage ($V_{Rx}$) and current ($I_{Rx}$) of the WPT system's receiver coil are shown in Fig. 10b.

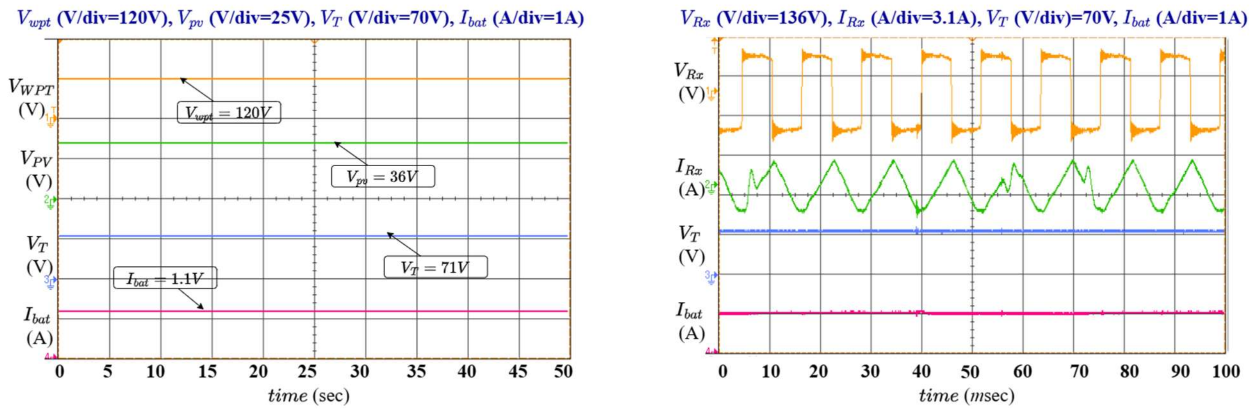


*(a)* *(b)*

*Figure 10. (a) Voltage and Current Waveforms during No step change in input parameters. (b) WPT system Receiver coil voltage ($V_{Rx}$) and current ($I_{Rx}$).*

*4.1.2. Case- I(b) (Step change in the Input voltages)*: In *Case-I(a)*, the stable EV charger operates under voltage variations from both the PV and WPT systems. In series-connected PV panels, partial shading due to clouds, trees, or other obstacles causes power mismatches. To mitigate this, bypass diodes activate, providing an alternate current path but reducing the overall PV voltage, leading to step voltage changes in the dual-input buck-boost (DIbB) converter. Despite these variations, the JAYA-optimized PI controller effectively regulates the charging current. A detailed analysis of this control action is shown in Fig. 12. In *Region-1*, one 6V panel is bypassed due to partial shading, reducing the PV voltage from 36V to 30V, while in *Region-2*, two panels are bypassed, further lowering the voltage to 24V. Nevertheless, the controller maintains stable charging. All these PV system voltage variations are replicated using a PV simulator in the developed system.

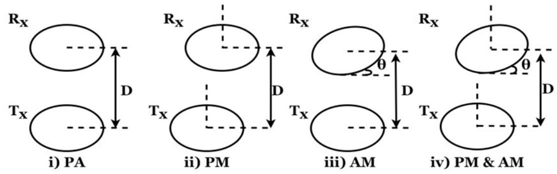


*Figure 11. Various Misalignments between the transmitter receiver coils in WPT system (i) Perfectly aligned (PA) (ii) Planar Misalignment (PM) (iii) Angular Misalignment (AM) (iv) Planar & Angular Misalignment (PM & AM)*

Further, *Regions-3, 4,* and *5* focus on the impact of misalignment in the WPT system. As the receiver (Rx) coil experiences positional shifts relative to the transmitter ($T_x$) coil as depicted in Fig. 11, variations in mutual inductance (*M*) cause fluctuations in the induced receiver voltage ($V_{WPT}$). These sudden voltage deviations could potentially disrupt the charging process. However, the JAYA-based controller continues to exhibit superior adaptability, ensuring that the charging current remains within the desired range under all misalignment conditions.

The effectiveness of this control approach is comprehensively illustrated in Fig. 12, while a detailed transient response analysis of all disturbance regions is presented in Table 3. The results affirm the robustness of the JAYA-optimized PI controller, demonstrating its capability to mitigate step voltage changes from PV shading and compensate for inductance variations in WPT-based power transfer ensuring seamless and stable EV charging.

*Table 3. Load Current Transient Response for PV Irradiation Variation and WPT Coil Misalignments.*

| Step changes in | Transient Regions | Peak Time (sec) | % Overshoot | Rise Time (sec) | Settling Time (sec) |
|---|---|---|---|---|---|
| PV system | Region-1 | 0.400 | -17.9 | 0.052 | 4.925 |
| | Region-2 | 0.375 | -14.04 | 0.175 | 2.450 |
| WPT system | Region-3 | 0.800 | 46.87 | 0.100 | 2.700 |
| | Region-4 | 0.375 | 14.00 | 0.075 | 1.950 |
| | Region-5 | 0.475 | -28.15 | 0.275 | 2.150 |

***Note**: A negative sign indicates undershoot.*

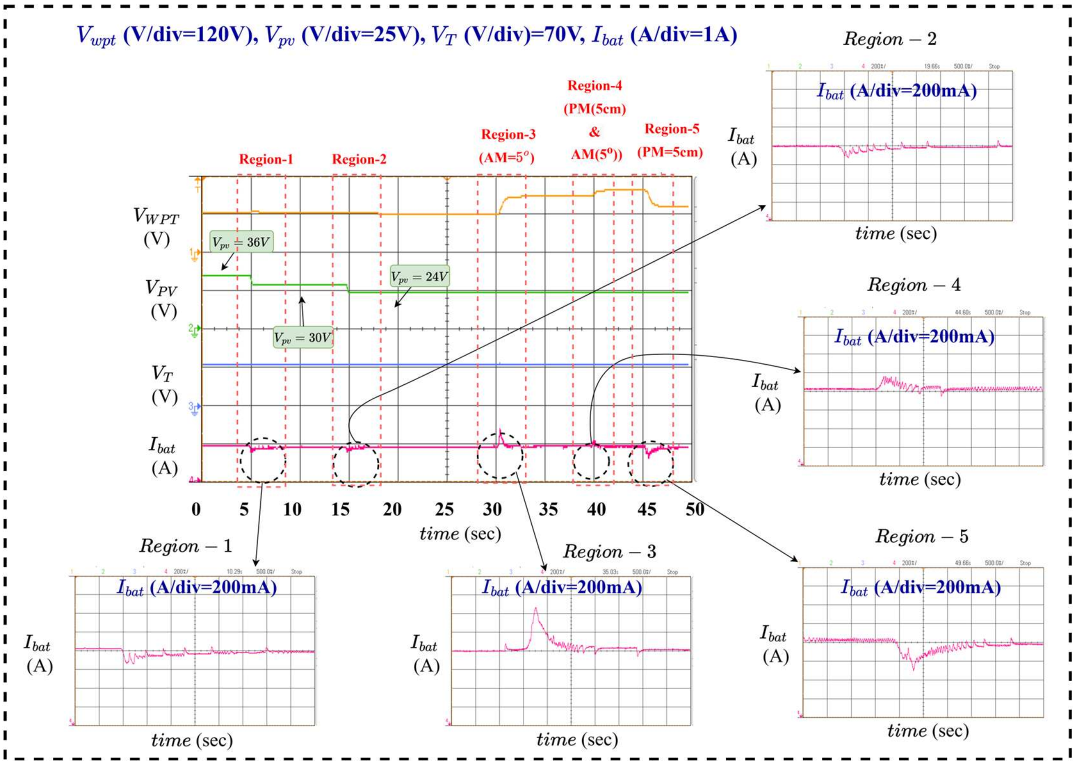


*Figure 12. Voltage and Current Waveforms during step change in inputs.*

*4.1.3. Case-I(c) (Change in the Load parameters)*: In this study, the output terminal voltage reference of the EV charger is subjected to abrupt variations, demonstrating the impact of adjustable terminal voltage in EV charging. Such adaptability is essential for accommodating different battery chemistries, charge levels, and power sources, thereby enhancing charging efficiency and prolonging battery lifespan. This flexibility is particularly crucial in multi-vehicle charging stations that must cater to diverse voltage requirements. To ensure stable voltage regulation and mitigate input fluctuations, an advanced control strategy is employed. Here, the JAYA algorithm-optimized PI controller is evaluated by analysing the charger's current response under dynamic voltage adjustments.

The performance assessment, illustrated in Fig. 13, is further detailed through a zoomed-in view of the terminal voltage and current, highlighting key regions where reference voltage transitions occur. In *Region-1*, the preset terminal voltage of 68V is suddenly increased to 71V, causing the charging current to rise from 0.6A, eventually stabilizing at approximately 1.1A. Similarly, in *Region-2*, when the voltage is reduced back to 67V, the charging current correspondingly drops to 0.4A. In *Region-3*, the terminal voltage is increased to 72V, leading to a controlled rise in charging current from 0.5A to around 1.4A. Despite these abrupt voltage variations, the smooth and stable transitions in the charging current demonstrate the robustness of the proposed control strategy in maintaining system stability and performance. These results validate the effectiveness of the JAYA-based PI controller in ensuring seamless charging operation, even under sudden voltage fluctuations, making it a reliable solution for next-generation EV charging applications.

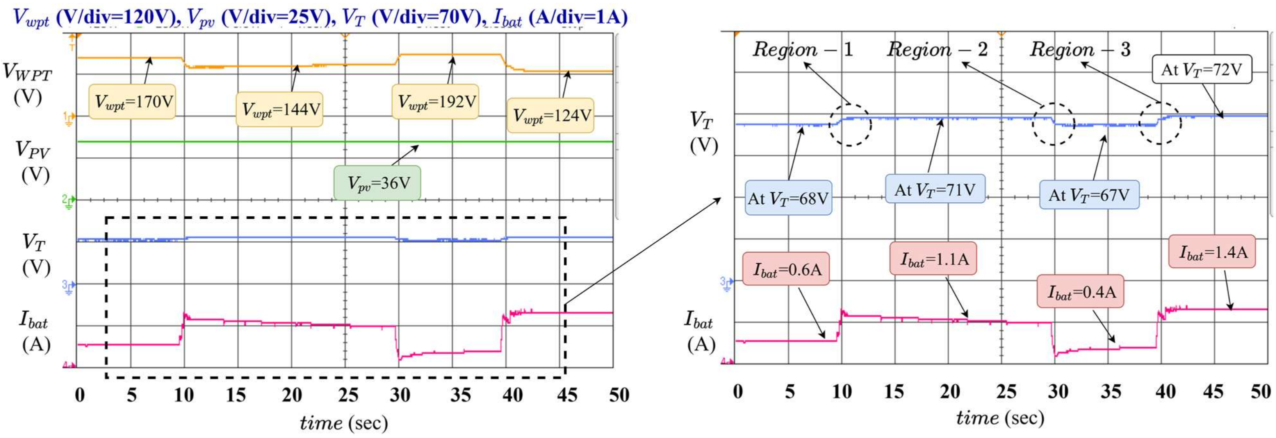


*Figure 13. Voltage and Current Waveforms during step change in battery charging voltage.*

*4.1.4. Case-II (Performance analysis of the proposed JAYA algorithm-based charger compared with the Zeigler-Nichols control method under various WPT system misalignments):* In this scenario, the performance of the proposed JAYA algorithm-based charger is compared with the conventional Zeigler-Nichols method of converter gain estimation, a standard approach for converter control, here we have adapted the ultimate gain and period method which has following steps,

1. Set $K_p$= 0 and $K_d$ = 0 to configure the system as a P controller only.
2. Gradually increase the proportional gain ($K_p$) until the system output shows sustained oscillations (constant amplitude).
3. Record the gain at which sustained oscillation occurs; this is the ultimate gain ($K_u$ = 0.53).
4. Measure the period of one full oscillation cycle; this is the ultimate period ($P_u$ = 0.005 seconds) as shown in Figure 14.

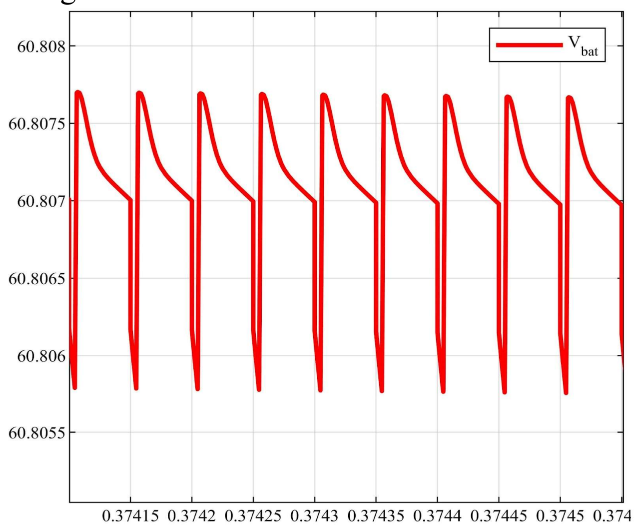


*Figure 14. Sustained oscillations of the converter output voltage for ultimate gain of $K_u$=0.53.*

5. Apply Ziegler-Nichols tuning rules for a PI controller:
   a) $K_p$= 0.45 × $K_u$ = 0.45 × 0.53 = 0.24
   b) $T_i$= $P_u$ / 1.2 = 0.005 / 1.2 = 0.0042 seconds
   c) $K_i$= $K_p$ / $T_i$ = 0.24 / 0.0042 = 57.14
6. Final PI controller parameters: $K_p$= 0.24; Ti = 0.0042 seconds; Ki= 57.14

The charger, initially operating in a stable state, is tested under voltage variations due to possible misalignments between the Rx coil and the Tx coil in the WPT system, as discussed earlier. Performance comparisons focus on the WPT system's voltage fluctuations, as observed in *Case-Ib*, where WPT system variations more significantly impact charger performance than PV voltage variations. The effects of these misalignments on the charging current are analyzed across various regions, as illustrated in Fig. 12. In *Region-1*, the *Rx* coil experiences angular misalignment with the *Tx* coil, causing an increase in receiver voltage and a reduction in receiver current, leading to a rise in charging current. This increase is effectively managed by the JAYA algorithm-optimized PI controller, as previously discussed. In *Region-2*, combined planar and angular misalignments in the receiver lead to further increases in receiver voltage at the cost of reduced receiver current. The controller subsequently restores the charging current to the reference value. Similarly, in *Region-3*, the Rx coil undergoes planar misalignment, and the proposed controller efficiently regulates the charging current. For clarity, a zoomed-in view of each region is provided in Fig. 15a for JAYA algorithm-based control and Fig. 15b for Zeigler-Nichols control with the control parameters calculated. To further clarify performance differences, transient parameters for each region are summarized in Table 4. Additionally, a bar graph in Fig. 16 illustrates a comparison of time-domain specifications for both control methods, clearly demonstrating the superior control stability offered by the proposed JAYA algorithm.

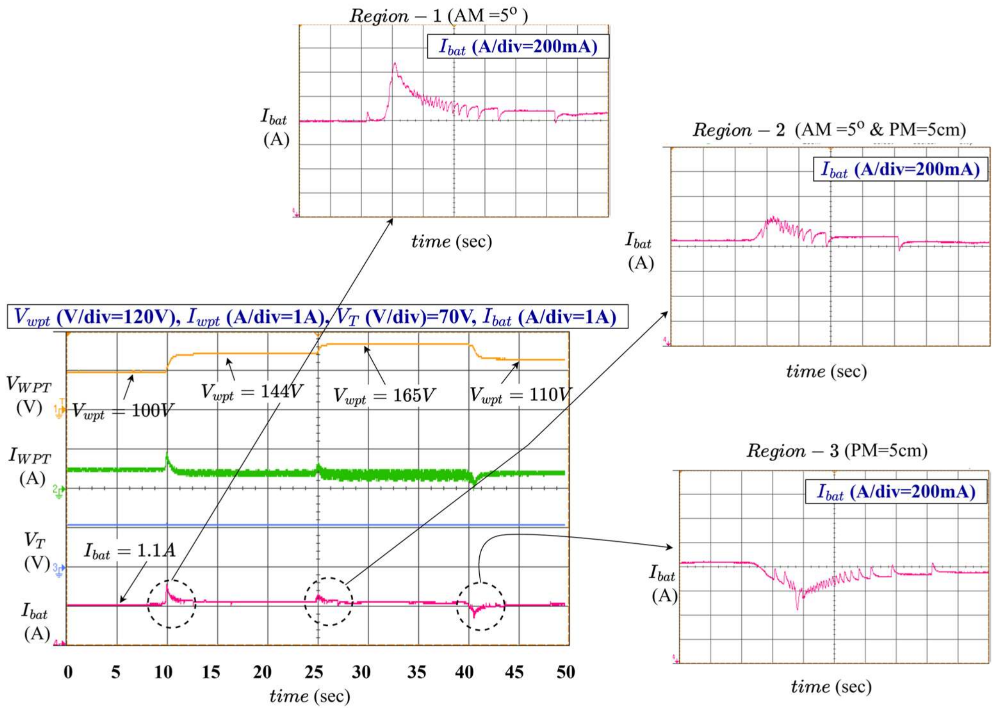


*(a)*

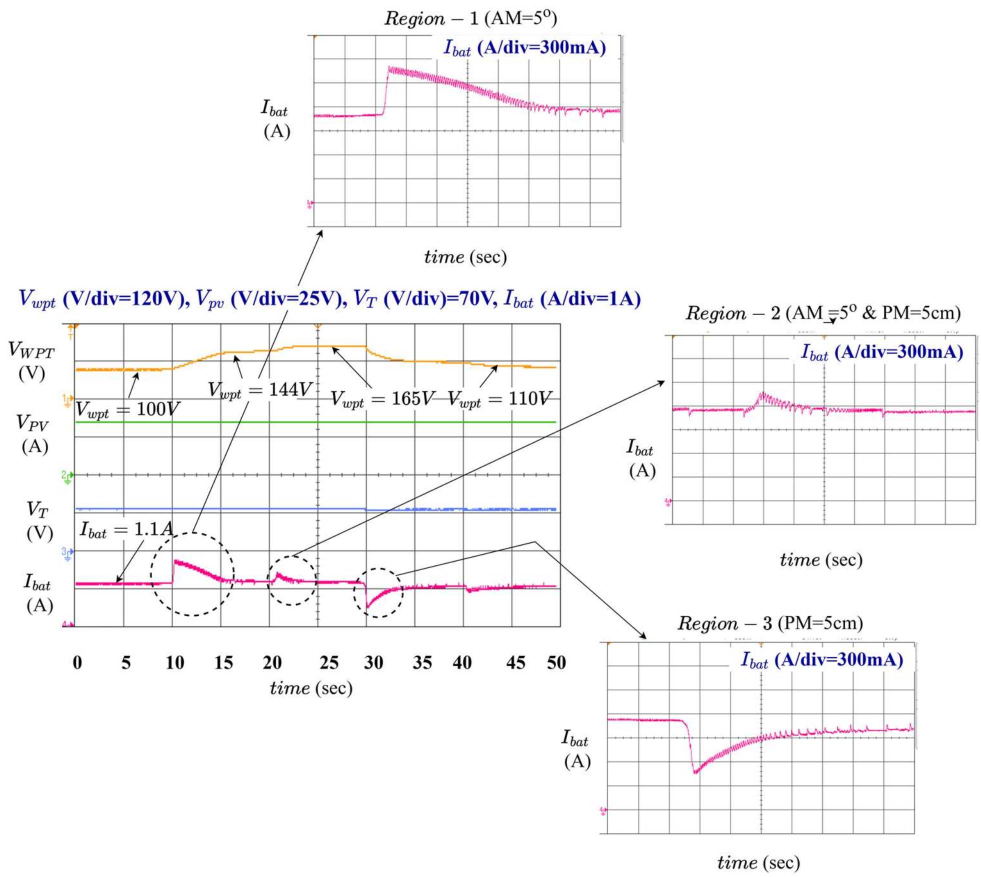


*(b)*

*Figure 15. Voltage and Current Waveforms with various misalignments in WPT input. (a) JAYA Algorithm. (b) Ziegler Nichols method.*

*Table 4. Transient Response Performance: Proposed Controller vs. Zeigler-Nichols Method under WPT Coil Misalignments.*

| Method of Control | Transient Regions | Peak Time (sec) | % Overshoot | Rise Time (sec) | Settling Time (sec) |
|---|---|---|---|---|---|
| JAYA Algorithm | Region-1 (AM-5◦) | 0.3500 | 39.04 | 0.0750 | 3.27 |
| | Region-2 (PM-5cm & AM-5◦) | 0.6000 | 20.01 | 0.0750 | 2.05 |
| | Region-3 (PM-5cm) | 0.9750 | -28.01 | 0.5000 | 2.875 |
| Zeigler-Nichols Method | Region-1 (AM-5◦) | 0.3750 | 47.05 | 0.1000 | 6.10 |
| | Region-2 (PM-5cm & AM-5◦) | 0.7250 | 21.59 | 0.0500 | 4.075 |
| | Region-3 (PM-5cm) | 0.6750 | -58.50 | 0.2750 | 4.275 |

***Note**: A negative sign indicates undershoot.*

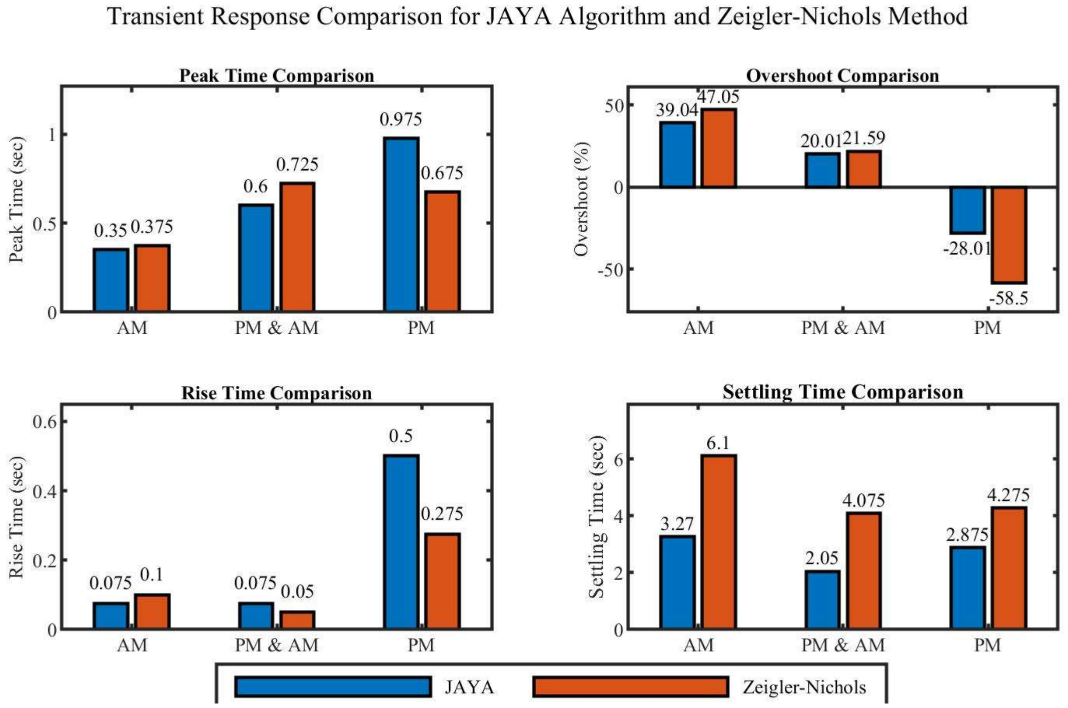


*Figure 16. Bar graph illustrating the comparative performance analysis of the JAYA algorithm-based control versus the Zeigler-Nichols method of control.*

## 5 CONCLUSIONS

With the growing adoption of electric vehicles (EVs), the development of reliable and efficient on-board charging systems has become increasingly important. This paper presents the design and evaluation of a feedback controller for a dual-input EV charger powered by photovoltaic (PV) and wireless power transfer (WPT) sources. The JAYA optimization algorithm is employed to tune the controller parameters, aiming to regulate the output voltage at a constant level throughout the charging process.System performance were assessed under varying conditions, including step changes in input power and coil misalignments in the WPT system. Compared to the conventional Ziegler-Nichols (Z-N) tuning strategy, the JAYA-tuned controller demonstrated significantly improved response characteristics. These included faster settling times, reduced overshoot, and enhanced system stability, particularly under fluctuating power supply from both PV and WPT sources. The ability to maintain constant voltage charging highlights the controller's effectiveness for hybrid energy-based EV charging systems.

However, the approach has certain limitations. When implemented in real-time hardware, algorithm-based control demands considerable computational resources and may introduce latency, potentially affecting system responsiveness. The performance is also sensitive to parameters such as population size and the number of iterations, which can influence convergence speed and control stability. Additionally, the integration of such algorithms increases system complexity and may require more advanced hardware, impacting cost and design effort. In conclusion, the JAYA-based controller, as demonstrated through hardware implementation, offers clear advantages over conventional tuning methods for dual-input EV chargers, particularly in achieving faster dynamic response and improved stability. Future work can focus on refining real-time adaptive strategies and optimizing algorithm efficiency to further enhance performance in practical applications.

## APPENDIX

*Table 5. Parameters of WPT System, and Buck-Boost Converter.*

| WPT System | | Buck-Boost Converter | |
|---|---|---|---|
| **Parameter** | **Value** | **Parameter** | **Value** |
| Wire type | Litz | Input Voltage Range | 36V to 200V |
| Coil turns | 28 | Output Voltage | 71V |
| Frequency (kHz) | 85 | Voltage Ripple | 0.1V |
| Self-inductance ($\mu$H) | 177 | Switching Frequency | 20kHz |
| Capacitor (nF) | 18.75 | Load Current | 2.4A |
| Length (cm) | 36 | Duty Cycle (Min) | 0.664 |
| Width (cm) | 36 | Duty Cycle (Max) | 0.262 |
| Coil shape | Square | Inductor Value | 3.8mH |
| | | Capacitor Value | 420µF |

## REFERENCES

[1] Rahman, I., Vasant, P. M., Singh, B. S. M., Abdullah-Al-Wadud, M., & Adnan, N. (2016). Review of recent trends in optimization techniques for plug-in hybrid, and electric vehicle charging infrastructures. *Renewable and Sustainable Energy Reviews*, *58*, 1039-1047.

[2] Manivannan, B., Kathirvelu, P., & Balasubramanian, R. (2023). A review on wireless charging methods–The prospects for future charging of EV. *Renewable Energy Focus*, *46*, 68-87.

[3] Birnie III, D. P. (2016). Analysis of energy capture by vehicle solar roofs in conjunction with workplace plug-in charging. *Solar energy*, *125*, 219-226.

[4] Balasubramanian, I. R., Ilango Ganesan, S., & Chilakapati, N. (2014). Impact of partial shading on the output power of PV systems under partial shading conditions. *IET power Electronics*, *7*(3), 657-666.

[5] Annaselvaraj, B., Nayak, P. S. R., Sundareswaran, K., & Simon, S. P. (2025). Systematic analysis and investigations on different coil structures with misalignments for WPT system. *e-Prime-Advances in Electrical Engineering, Electronics and Energy*, *12*, 100959.

[6] Pradhan, S. K., & Chakraborty, B. (2022). Battery management strategies: An essential review for battery state of health monitoring techniques. *Journal of energy storage*, *51*, 104427.

[7] Dhananjaya, M., & Pattnaik, S. (2021). Review on Multi-Port DC–DC Converters. *IETE Technical Review*, *39*(3), 586–599. https://doi.org/10.1080/02564602.2021.1882343.

[8] Athikkal, S., Kumar, G. G., Sundaramoorthy, K., & Sankar, A. (2017). Performance analysis of novel bridge type dual input DC-DC converters. *IEEE Access*, *5*, 15340-15353.

[9] Athikkal, S., Kumar, G. G., Sundaramoorthy, K., & Sankar, A. (2017). Performance analysis of novel bridge type dual input DC-DC converters. *IEEE Access*, *5*, 15340-15353.

[10] Kumaravel, S., Kumar, G. G., Veeranna, K., & Karthikeyan, V. (2018, December). Novel non-isolated modified interleaved DC-DC converter to integrate ultracapacitor and battery sources for electric vehicle application. In *2018 20th National Power Systems Conference (NPSC)* (pp. 1-6). IEEE.

[11] Kumar, L., & Jain, S. (2013). Multiple-input DC/DC converter topology for hybrid energy system. *IET Power Electronics*, *6*(8), 1483-1501.

[12] Appikonda, M., & Kaliaperumal, D. (2019). Modelling and control of dual input boost converter with voltage multiplier cell. *IET Circuits, Devices & Systems*, *13*(8), 1267-1276.

[13] Colalongo, L., Dotti, D., Richelli, A., & Kovács-Vajna, Z. M. (2017). Non-isolated multiple-input boost converter for energy harvesting. *Electronics Letters*, *53*(16), 1132-1134.

[14] Guru Kumar, G., Sundaramoorthy, K., Athikkal, S., & Karthikeyan, V. (2019). Dual input superboost DC–DC converter for solar powered electric vehicle. *IET Power Electronics*, *12*(9), 2276-2284.

[15] Reddy, M. S. K., Kalyani, C., Uthra, M., & Elangovan, D. (2015). A small signal analysis of DC-DC boost converter. *Indian Journal of Science and Technology*, *8*, 1.

[16] Kamalapathi, K., Srinivasa Rao Nayak, P., & Tyagi, V. K. (2021). Design and implementation of dual-source (WPT+ PV) charger for EV battery charging. *International Transactions on Electrical Energy Systems*, *31*(11), e13084.

[17] Hosseinnataj, S., Yazdani, M., Shekari, M., Jani, M., & Adabi, J. (2023, January). Bidirectional DISO DC-DC converter based on Lyapunov control strategy. In *2023 14th Power Electronics, Drive Systems, and Technologies Conference (PEDSTC)* (pp. 1-5). IEEE.

[18] Hosseini, A., Hosseinnataj, S., & Adabi, J. (2024, May). Bidirectional DISO DC-DC Converter Based on Fixed-Frequency Sliding Mode Control Strategy. In *2024 32nd International Conference on Electrical Engineering (ICEE)* (pp. 1-5). IEEE.

[19] Hosseini, A., Hosseinnataj, S., Mehrasa, M., & Adabi, J. (2025, February). Super Twisting Control Strategy Implemented on a Bidirectional DISO DC-DC Converter. In *2025 12th Iranian Conference on Renewable Energies and Distributed Generation (ICREDG)* (pp. 1-6). IEEE.

[20] Younesi, A., Farajpour, R., Hosseinnataj, S., Adabi, J., & Mousavi, S. Y. M. (2024, December). A Backstepping Control with Nonlinear Disturbance Observer for BDISO Converter. In *2024 14th Smart Grid Conference (SGC)* (pp. 1-6). IEEE.

[21] Demir, M. H., & Demirok, M. (2023). Designs of particle-swarm-optimization-based intelligent PID controllers and DC/DC Buck converters for PEM fuel-cell-powered four-wheeled automated guided vehicle. *Applied Sciences*, *13*(5), 2919.

[22] Hsiao, Y. T., Chuang, C. L., & Chien, C. C. (2004, September). Ant colony optimization for designing of PID controllers. In *2004 IEEE International Conference on Robotics and Automation (IEEE Cat. No. 04CH37508)* (pp. 321-326). IEEE.

[23] Prabakar, K., & Li, F. (2012). Application of genetic algorithm for the improved performance of boost converters. *IFAC Proceedings Volumes*, *45*(21), 85-90.

[24] Rao, R. V., & Waghmare, G. G. (2017). A new optimization algorithm for solving complex constrained design optimization problems. *Engineering Optimization*, *49*(1), 60-83.

[25] Migallón, H., Jimeno-Morenilla, A., Sánchez-Romero, J. L., & Belazi, A. (2020). Efficient parallel and fast convergence chaotic Jaya algorithms. *Swarm and Evolutionary Computation*, *56*, 100698.

[26] Sain, D., Swain, S. K., & Mishra, S. K. (2018). Real time implementation of optimized I-PD controller for the magnetic levitation system using Jaya algorithm. *IFAC-PapersOnLine*, *51*(1), 106-111.

[27] Kindl, V., Frivaldsky, M., & Skorvaga, J. (2021). Theoretical and Practical Design Approach of Wireless Power. *Wireless Power Transfer: Recent Development, Applications and New Perspectives*, 43.